INSTITUTE OF PHYSICS PUBLISHING BIOINSPIRATION & BIOMIMETICS

Bioinsp. Biomim. **1** (2006) S35–S41 doi:10.1088/1748-3182/1/4/S05

Locomotion with flexible propulsors: II. Computational modeling of pectoral fin swimming in sunfish

Rajat Mittal[1], **Haibo Dong**[1], **Meliha Bozkurttas**[1], **GeorgeV Lauder**[2] **and Peter Madden**[2]

[1] Department of Mechanical and Aerospace Engineering, The George Washington University, Washington, DC, USA
[2] Harvard University, Cambridge, MA, USA

E-mail: mittal@gwu.edu

Received 1 August 2006
Accepted for publication 22 November 2006
Published 22 December 2006
Online at stacks.iop.org/BB/1/S35

Abstract
This paper describes a computational fluid dynamics (CFD) based investigation of the pectoral fin hydrodynamics of a bluegill sunfish. The pectoral fin of this fish undergoes significant shape-change during its abduction–adduction cycle and the effect of this deformation on the thrust performance remains far from understood. The current study is part of a combined experimental–numerical approach wherein the numerical simulations are being used to examine features and issues that are not easily amenable to the experiments. These numerical simulations are highly challenging and we briefly describe the computational methodology that has been developed to handle such flows. Finally, we describe some of the key computational results including wake vortex topologies and hydrodynamics forces.

1. Introduction

The focus of the current study is the hydrodynamics of highly deformable pectoral fins that are used for propulsion and maneuvering by fish. The particular fish of interest here is the bluegill sunfish (*Lepomis macrochirus*) shown in figure 1. These are highly maneuverable bony fishes which have been the subject of a number of previous experimental analyses of locomotor function (Drucker and Lauder 1999, 2000, 2001a, 2001b, Jayne *et al* 1996, Gibb *et al* 1994) and serve as excellent experimental subjects for an integrated approach to understanding the function of fish fins, deriving the principles of fish fin function, and applying these principles to construction of a biomimetic robotic fin for use in maneuvering autonomous underwater vehicles (AUVs).

Sunfish are able to execute highly effective yaw maneuvers using only their pectoral fins, and at speeds of less than 1.1 body length per second use only their pectoral fins for propulsion. Sunfish pectoral fins are also representative of the structure of the vast majority of bony fish fins (Lauder *et al* 2002, 2003, 2005) in possessing bony fin rays joined by a thin collagenous membrane.

The motion of the sunfish pectoral fin during propulsion has been quantified by Lauder *et al* (2006) using two calibrated high-speed video cameras recording simultaneously at 250 and 500 fps with 1024 × 1024 pixel resolution. Digitizing up to 300 points per time step in 3D and using approximately 20 time increments per fin beat allowed detailed reconstruction of 3D fin motion. Pectoral fin motion in three dimensions is very complex (figure 2) and involves: (1) simultaneous movement of the upper and lower fin edges away from the body, forming two simultaneous leading edges, (2) strong cupping of the fin as it moves away from the body, (3) a wave of bending that moves spanwise along the upper edge of the fin at higher than free-stream flow velocity, (4) 'dimpling' of the upper fin surface behind the leading edge, (5) substantial reorientation of the fin base and rotation of the fin (figure 2) and (6) significant area changes during the fin beat (Lauder *et al* 2006).

For measurement of the fluid flow, the experiments have utilized a transverse light sheet which provides a complete transect of flow in the wake. By using two simultaneous high-resolution (1024 × 1024 pixel) high-speed video cameras

Figure 1. Bluegill sunfish showing the right pectoral fin extended from the body.

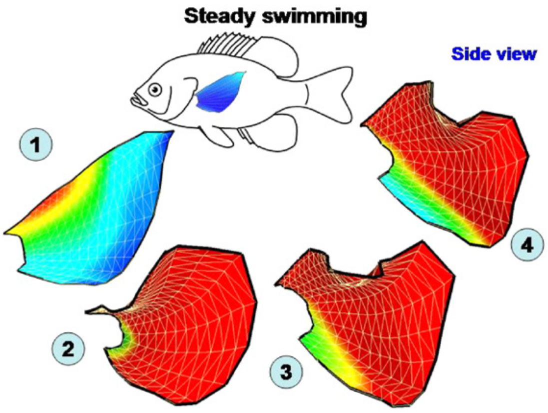

Figure 2. Conformations of the sunfish pectoral fin at four times (0, 0.6τ, 0.7τ, 0.75τ) during the fin beat cycle (of period τ) in steady forward locomotion. Color reflects distance from the body, with blue indicating positions near the body, and red positions away from the body.

operating at 500 fps, we were able to obtain stereo-DPIV data to simultaneously measure velocity components within the light sheet. DPIV data from the transverse light sheet during steady propulsion demonstrate a number of distinctive vortical features which have been described in Lauder *et al* (2006). The overall picture that emerges from experimental hydrodynamic analyses of freely-swimming sunfish is that fin flexibility, especially independent control of the upper and lower fin edges, is critical to propulsion. However, there are a number of aspects of the flow that are not amenable to experimental measurement. Some of these limitations are inherent to all experiments and some are connected to the fact that these measurements are being done on a live animal. The primary aspect in the former category is the inability to simultaneously measure flow velocity components and pressure which vary rapidly in space and time. In the latter are the obvious difficulties of performing experiments that are highly repeatable as well as making measurements (such as surface measurements) which could potentially change the normal behavior of the subject. It is in these aspects that CFD can complement experimental investigations since CFD is not subject to any of these shortcomings (Mittal 2004). Another key strength of CFD is that it allows us to examine ‘what if’ type of questions which can sometimes lead to excellent insights into the underlying physical mechanisms. In the following sections we describe a CFD effort to study the hydrodynamics of the bluegill sunfish pectoral fin. We first describe a relatively new CFD methodology that we have developed for simulating such flows and this is followed by a discussion of our simulations.

2. CFD methodology

Computational modeling of such unsteady flows in which the propulsor is changing both shape and area is an extremely challenging proposition. For the particular fish which is the subject of the current study, the Reynolds number based on fish body length is $O(10^4)$. At this Reynolds number, the attached flow over the body is most likely laminar but is expected to transition rapidly to turbulence in regions of flow separation which might occur downstream of appendages. The pectoral fin which is the focus of the current study is highly deformable, has a complex planform and undergoes complicated motions. The flow over the fin can be characterized in terms of a Stokes frequency parameter ($S = \omega A l/\nu$) where ω, A and l are the fin angular frequency, amplitude and length respectively; values of this parameter are $O(10^3)$ which is again in the range where laminar attached flow would quickly transition to turbulence post separation. Thus, the computational modeling approach has to handle a wide variety of flow conditions. The motion of the pectoral fin is the key to the thrust generation and therefore, the computational method has to be able to include moving boundaries. The flow and thrust production is dominated by unsteady and vortex-based mechanisms such as added-mass effects, dynamic stall, vortex shedding, vortex pairing, vortex–body and vortex–fin interactions and therefore, the numerical method employed should have the ability to adequately resolve these features in both time and space. Finally, in general, two-way coupled fluid–structure interaction between the fin and the fluid plays a major role in determining the final conformation of the pectoral fin and the ability to be able to solve this coupled problem would allow us to address a number of interesting problems related to the role of passive deformation on the flow and thrust. However, in the current study, the focus is on modeling the hydrodynamics of the fin with motion prescribed based on experiments and the fluid–structure interaction problem is not addressed in the computational model.

In order to address this problem in all its complexity, a finite-difference-based immersed boundary methodology (Mittal and Iaccarino 2005) is used in the current simulations. The key feature of this method is that simulations with complex boundaries can be carried out on stationary, body non-conformal Cartesian grids and this eliminates the need for remeshing algorithms that are usually employed with conventional Lagrangian body-conformal methods (Ramamurti *et al* 2002). Further details regarding the solver and immersed boundary methodology can be found in Dong *et al* (2006) and application of the current solver to a large variety of flows can be found in Dong *et al* (2006), Kotapati *et al* (2006), Byrganhalli and Mittal (2006) and Mittal *et al* (2006). Here we describe some salient features of the solver with particular focus on the computational/modeling issues that are unique to the current flow configuration.

The governing equations that are solved are the three-dimensional Navier–Stokes equations, which in a non-dimensional form are given by:

$$\begin{aligned}\frac{\partial u_i}{\partial x_i} &= 0\\ \frac{\partial u_i}{\partial t}+\frac{\partial u_i u_j}{\partial x_j} &= -\frac{\partial p}{\partial x_i}+\frac{1}{Re}\frac{\partial^2 u_i}{\partial x_j \partial x_j}\end{aligned} \qquad (1)$$

where i and $j = 1, 2$ and 3 correspond to x, y and z coordinates as shown in figure 4, respectively and there is a sum over the repeated index. Re is the Reynolds number defined based on appropriate length and velocity scales. In the above equations, u_i is the instantaneous velocity component in the i direction, p is the pressure and t is the non-dimensional time. The equations have been non-dimensionalized by appropriate velocity and length scales. The equations are integrated in time using the fractional-step method (Chorin 1967) which leads to an advection–diffusion equation and a pressure Poisson equation. In the current solution procedure, the convective terms in the advection–diffusion are discretized using an explicit Adams–Bashforth scheme while the diffusive terms are modeled with an implicit Crank–Nicolson procedure. The spatial derivatives have been discretized with a second-order accurate, central-difference scheme on a collocated finite-difference stencil. Thus, both of the discretized equations to be solved can be written down as:

$$[A]\{\phi^{n+1}\} = \{R\} \qquad (2)$$

where ϕ is a generic flow variable that corresponds to velocity and pressure for the advection–diffusion and pressure Poisson equations respectively, $[A]$ is the banded matrix that represents the linear operator for the corresponding equation and $\{R\}$ is the corresponding source term. The above equations are solved for all the nodes of the Cartesian grid that lie in the fluid and the issue now is to devise a way of incorporating the effect of the immersed boundary on the fluid. For body-conformal grids, this is done by appropriately modifying equation (2) for grid nodes adjacent to the boundary so as to incorporate the appropriate boundary conditions (non-slip, no-penetration etc). However, in the context of a body non-conforming Cartesian grid, this process is not straightforward and in the following we describe how this is accomplished in the current solver.

2.1. Immersed boundary method

The basic concept of the current immersed boundary method is to compute the flow variables for the ghost cells (GC), such that boundary conditions on the immersed boundary in the vicinity of the ghost cells are satisfied while preserving second-order accuracy. Ghost cells are those cells whose centers lie inside (or on the other side of) the immersed body and have at least one neighboring cell that lies outside (or on the opposite side of) the immersed body. The process begins by constructing the surface of the immersed boundary. In the current solver, the immersed boundary is made up of a number of closely spaced marker points (or vertices in 3D) connected by linear segments (or triangular elements in 3D) that represent the boundary of the immersed geometry. A non-conformal Cartesian grid is then generated around the body followed by a procedure that identifies the ghost cells. The schematic in figure 3 shows the designation of the cells into the various categories.

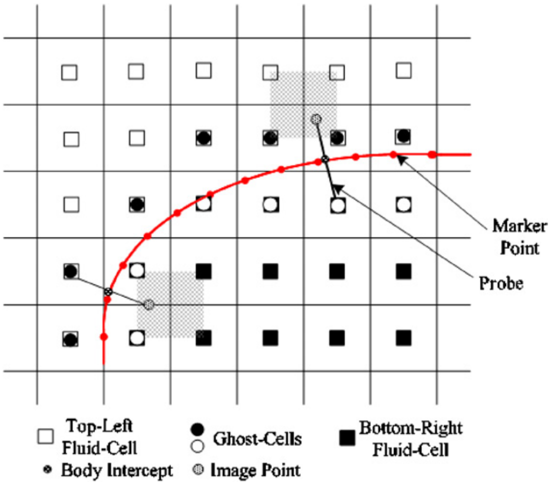

Figure 3. Designation of various nodes on the grid for membranous immersed structure.

Following the identification of the ghost cells a probe is extended from these cells to the immersed boundary such that it intersects normal to the immersed boundary. The intersection of the probe on the immersed boundary is called the boundary intercept (BI) and is the location where the boundary conditions will be satisfied. Next, the probe extends further into the fluid to a distance equal to the distance between the ghost cell and the boundary-intercept point. The location at the end of the probe is referred to as the image point (IP). Four (eight in 3D) cell nodes that surround the image point are then identified and a bi-linear (tri-linear in 3D) interpolation is employed to express the value of a generic flow variable ϕ at the image point, as follows:

$$\phi_{IP} = \sum \beta_i \phi_i \qquad (3)$$

where i extends over all the surrounding nodal points and β's are the interpolated weights corresponding to the nodes surrounding the image point. All of the information regarding the local geometry of boundary and its placement relative to the mesh is incorporated into these weights. The flow variables at the ghost cell are then computed using the values from the image point and boundary-intercept point which line on the normal probe via a second-order interpolation. Thus, for a Dirichlet boundary condition, the following equation for the ghost cell,

$$\phi_{GC} = 2\phi_{BI} - \phi_{IP} = 2\phi_{BI} - \sum \beta_i \phi_i \qquad (4)$$

is solved in conjunction with equation (2) and a similar expression can be developed for a Neumann boundary condition also. The effect of the boundary is therefore

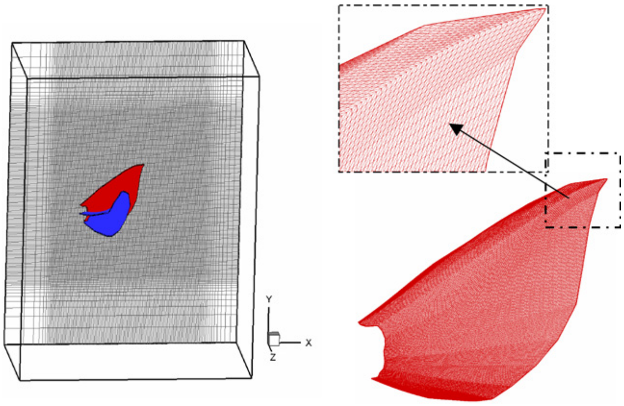

(*a*) (*b*)

Figure 4. (*a*) Grid and domain employed for the pectoral fin simulations. (*b*) High-density surface mesh with about 15 000 triangular elements used to define the pectoral fin.

incorporated into the equation for the ghost cell and the entire system of equations is transferred onto and solved on a Cartesian grid. Note that as the boundary moves, the grid remains unaltered. All that is needed is to renew the designations of the cells given the new location of the immersed boundary and to re-compute the β weights for the ghost cells. Once this is done, the discretized equations (2) and (4) can again be solved to obtain the flow at the new time step. It should be noted that the solution of pressure Poisson equation (PPE) is the most time consuming part of the solution algorithm. In the current solver an efficient multigrid methodology is used which is well suited for use in conjunction with the immersed boundary method. Performance results for the multigrid method can be found in Bozkurttas *et al* (2005).

For membranous bodies such as the fish pectoral fin, one has to deal with the situation that there are two sets of ghost cells on each side of the membrane and furthermore, that all ghost cells are simultaneously also regular fluid cells. Thus each such cell has two governing equations and two corresponding values. In order to handle this, we have developed a strategy wherein the ghost values are stored in auxiliary arrays and pointers are used to access this auxiliary storage when needed. Figure 4(*a*) shows a typical grid and computational domain employed in the current study. As can be seen, higher grid resolution is used around the fin in order to capture accurately the vortex dynamics in this region. Figure 4(*b*) shows the high-density surface mesh made up of triangular elements that is used to specify the surface of the pectoral fin. The high resolution of this mesh ensures that we adequately capture the complex geometrical conformation of the fin during its entire cycle.

3. Results

The hydrodynamic performance of the bluegill's pectoral fin is examined by carrying out a set of simulations using experimentally recorded kinematics. In these simulations, the Strouhal number (defined as $St = L_S f/U_\infty$ where L_S, f and U_∞ are the spanwise size of the fin, fin flapping frequency and fish forward velocity respectively) is 0.54 and matches that in the experiment. The Reynolds number (defined as $Re_\infty = U_\infty L_S/\nu$) is set to 1440 which is about one-fourth of that in the experiment. The Reynolds number has a relatively weak effect on the hydrodynamics and thrust of these types of flows (Triantafyllou *et al* 2004, Dong *et al* 2006) and the lower Reynolds number chosen here allows us to perform these simulations with smaller grids while still providing insights into the hydrodynamics. The nominal grid size employed in the current simulations is 153 ×161 ×113 which is about 2.78 million grid points. At the inflow boundary, we provide a constant uniform inflow velocity boundary condition. Instead of the fish body, for simplicity we include a vertical wall next to the fin. This is justifiable given the highly streamlined shape of the fish body and the fact that the fin is located nearer to the front of the body where the boundary layer on the body is expected to be attached and relatively thin. However, simulations including the fish body are planned to precisely quantify the effect of the body on the fin performance. Comprehensive studies have been carried out to assess the effect of the grid resolution and domain size on the salient features of the flow and also to demonstrate the accuracy of the nominal grid size (Bozkurttas *et al* 2006).

Figures 5(*a*)–(*c*) show the side view of the vortex structures, the iso-surfaces of the eigenvalue imaginary part of the velocity gradient tensor (Soria and Cantwell 1993), for the pectoral fin at three different times during one

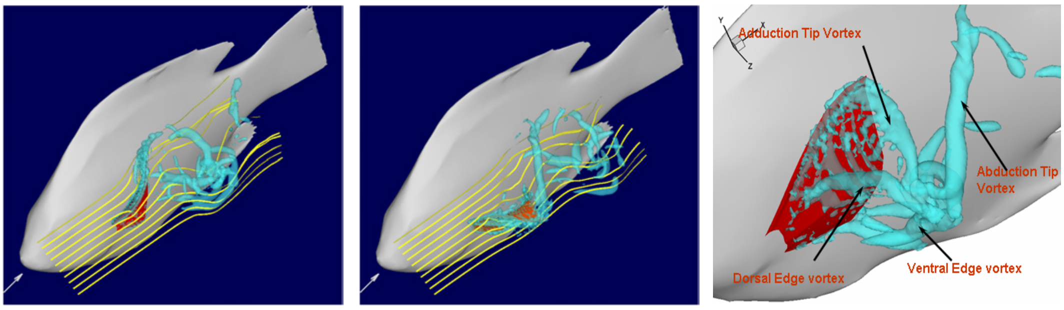

(*a*) (*b*) (*c*)

Figure 5. Computed wake structures for complete motion of fish pectoral fin.

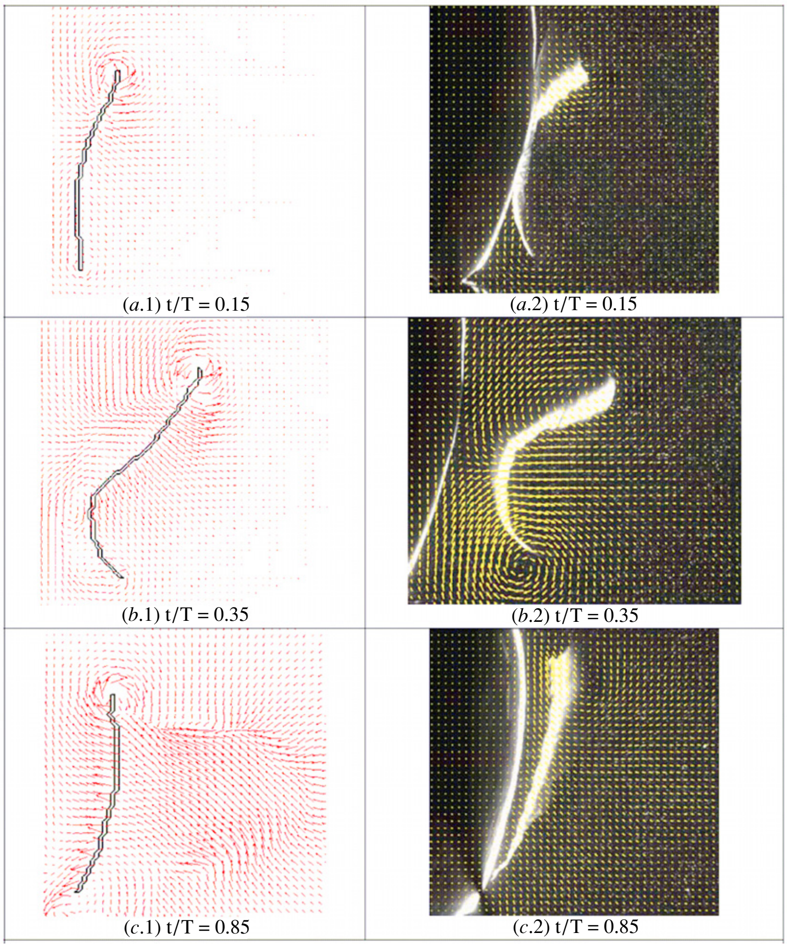
(*a*.1) t/T = 0.15
(*a*.2) t/T = 0.15
(*b*.1) t/T = 0.35
(*b*.2) t/T = 0.35
(*c*.1) t/T = 0.85
(*c*.2) t/T = 0.85

Figure 6. Vector plots on a streamwise plane located at 67% from the root of the fin (a.1, b.1, c.1 from CFD results and a.2, b.2, c.2 from PIV measurements).

complete cycle of motion, where x and z are the streamwise and spanwise directions respectively. Also shown are instantaneous streamlines around the fin. The body of the fish is shown for viewing purpose only and is not included in the simulations. The set of three iso-surface plots shows a very complex system of vortices being generated by the fin as it moves through a complete cycle. In particular, during the abduction stroke which is shown in figures 5(*a*) and (*b*), we see the formation of a dorsal leading-edge vortex which stays attached to the leading edge throughout the abduction stage. In addition at the spanwise tip, the leading-edge vortex joins with a tip vortex that starts to extend into the wake. At the final stage in the abduction shown in figure 5(*b*), the tip vortex is seen to extend quite a distance from the spanwise tip and a closer examination shows that it is made up of spiraling vortex filaments typical of wing-tip vortices from lifting wings (Maxworthy 1979, Van Dyke 1988).

During the adduction stroke the entire fin initially moves backward almost simultaneously and this leads to a very different vortex structure. Figure 5(*c*) shows the vortex structures generated by the end of the adduction stroke and in addition to the spanwise tip-vortex formed during the abduction stroke (and labeled as 'abduction tip vortex'), three other distinct vortices are formed. First is the adduction-induced spanwise tip vortex which is marked as 'adduction tip vortex' in the figure. In addition there is the detached dorsal leading-edge vortex and the detached ventral leading-edge vortex. Thus the vortex systems during the two stages of the cycles are very different from each other; what the effect of this asymmetry is on the forces production on the fin will be examined in the later sections of this paper.

PIV measurements taken of the flow past the fish pectoral fin in steady swimming are used for qualitative comparison with the current simulations. It should be noted that the fish fin kinematics which are employed in the CFD are not measured simultaneously with the PIV measurements and therefore perfect correlation with the experiments is not expected. Nevertheless, we expect the numerical simulations to match the key topological features of the flow. Figures 6(*a*)–(*c*) show flow velocity vectors from CFD results and PIV measurements at a streamwise plane shown in figure 5(*c*) which is located roughly $(2/3)L_S$ downstream from the fin root. Figure 6(*a*) corresponds to an early time in the cycle where the fin initiates its motion away from the body and simultaneously undergoes a 'cupping' motion that rapidly accelerates its upper and lower fin tips. A consequence of this

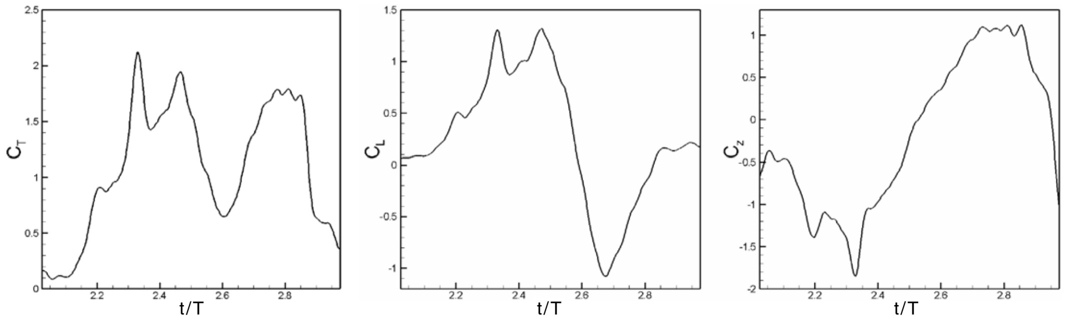

(*a*) (*b*) (*c*)

Figure 7. Computed temporal variation force coefficients for the pectoral fin at $Re = 1440$. (*a*) Thrust coefficient, (*b*) lift coefficient, (*c*) spanwise force coefficient.

rapid acceleration is the formation of two tip vortices where the one at the top is stronger than that at the bottom (as shown in figure 5). Figure 6(*b*) is roughly at $1/3$rd of the cycle and at this time instant CFD and PIV show the presence of two tip vortices. Finally, figure 6(*c*) shows the time instant where the cycle is almost complete and the fin moves back to the body. At this instant, the PIV measurements show only one vortex which is attached to the upper tip and the CFD simulations also reproduce similar behavior. Overall, the comparison between the experiments and CFD is quite reasonable and improves our confidence level in the fidelity of the numerical simulations. More quantitative comparisons between experiments and CFD will be presented in the future.

One key quantity that the simulations can provide is the hydrodynamic force that is produced by the fin. The force coefficient C_F for a given force F is computed as $C_F = F/(1/2)\rho U_\infty^2 A_{\text{fin}}$, where A_{fin} is the nominal fin area. Figure 7(*a*) shows the temporal variation of the thrust coefficient for the third cycle. In our study, the flow reaches a stationary state in about two cycles and there is no significant cycle-to-cycle change in the forces beyond this point. It can be observed in the plots that not only are there two large peaks of thrust during the full cycle, positive thrust is produced during all phases of the cycle. This behavior is very different from behavior exhibited by canonical rigid flapping foils where drag is usually produced at some phases in the cycle (Mittal *et al* 2003, Dong *et al* 2006). This finding hints at the superior thrust-generation capability of this highly deformable fin. Figures 7(*b*) and (*c*) show the other two components of the forces produced by the fin and a number of interesting observations can be made regarding these plots. First, peak magnitudes of these transverse force components are smaller than the peak thrust. This is also highly unexpected since all existing data on rigid flapping foils (Mittal *et al* 2003, Mittal 2004, Lewin and Haj-Hariri 2003, Isogai *et al* 1999, Triantafyllou *et al* 2004, Dong *et al* 2006) show that the peak thrust is significantly smaller than the peak lift and or spanwise force. This is a clear indication of what we expect to be a relatively high propulsive efficiency for this fin. Second, both these forces have positive and negative variations in a cycle that are of similar magnitudes and this implies that the mean values of these force components will be small.

Table 1. Mean force coefficients for fish pectoral fin in steady forward motion.

Thrust coefficient	Lift coefficient	Spanwise force coefficient
1.05	0.25	−0.21

Table 1 shows the mean values of the hydrodynamic force coefficients produced by the fin at the third flapping cycle at $Re = 1440$. The mean thrust coefficient for this case is found to be 1.05. The mean values of lift and spanwise force components over one cycle are small; 0.25 for the lift coefficient and -0.21 for the spanwise force coefficient. Thus, the clear asymmetry of the stroke kinematics and associated vortex dynamics is not manifested in the force coefficient which is quite surprising. The low mean values of the transverse forces are important for the fish since they allow the fish to minimize transverse body oscillations as it propels itself forward in a steady manner. Among other things, this provides the fish with a relatively steady platform from which it is able to visually survey its surroundings. From the point of view of the development of biomimetic flapping foils, the current simulations provide a first glimpse of the inherent advantages that deformable flapping foils offer over conventional rigid flapping foils. Guided by the current experimental–numerical effort, deformable flapping foils are currently being engineered and tested (Lauder *et al* 2005, Tangorra *et al* 2006) and results of these tests will be available in the near future.

4. Summary

Numerical simulations have been used to study the hydrodynamics of the highly deformable pectoral fin of a bluegill sunfish. The simulations complement a companion experimental study (Lauder *et al* 2006) and help in gaining insight into the performance of the fin. These simulations are extremely challenging due to the need to model the flow accurately at relatively high Reynolds number and with a highly deformable, membranous fin. In the current paper, we have used a new Cartesian-grid-based immersed-boundary solver which is successfully able to simulate the flow in all its complexity. The simulations provide information regarding the vortex dynamics, surface forces and hydrodynamic forces which supplement the information obtained from the experiments and help us gain a better understanding of the effect of the fin kinematics on the hydrodynamic performance. The insights obtained here are being used to design a bio-inspired engineered fin that will be appropriate for propelling a small autonomous undersea vehicle (Tangorra *et al* 2006).

Acknowledgments

This work was supported by ONR-MURI Grant N00014-03-1-0897 monitored by Dr Thomas McKenna. We would also like to acknowledge collaboration with Dr Ian Hunter and Dr James Tangorra at MIT and helpful comments from two anonymous reviewers on the original manuscript.

References

Bozkurttas M, Dong H, Mittal R, Madden P and Lauder GV 2006 Hydrodynamic performance of deformable fish fins and flapping foils *AIAA 2006-1392 (Reno, NV)*

Bozkurttas M, Dong H, Mittal R, Madden P, Lauder G and Najjar F 2005 Simulation of flow past flapping foils with active chordwise deformation AIAC 2005-034: *Ankara Int. Aerospace Conf. (Turkey: Middle East Technical University)*

Bozkurttas M, Dong H, Seshadri V, Mittal R and Najjar F 2005 Towards numerical simulation of flapping foils on fixed Cartesian grids *AIAA 2005-0079 (Reno, NV)*

Byrganhalli R and Mittal R 2006 Numerical study of large aspect ratio synthetic jets *AIAA 2006-0315 (Reno, NV)*

Chorin A J 1967 A numerical method for solving incompressible viscous flow problems *J. Comput. Phys.* **2** 12–26

Dong H, Mittal R, Bozkurttas M and Najjar F 2005 Wake structure and performance of finite aspect-ratio flapping foils *AIAA 2005-0081 (Reno, NV)*

Dong H, Mittal R and Najjar F 2006 Wake topology and hydrodynamic performance of low aspect-ratio flapping foils *J. Fluid Mech.* **566** 309–43

Drucker E G and Lauder G V 1999 Locomotor forces on a swimming fish: three-dimensional vortex wake dynamics quantified using digital particle image velocimetry *J. Exp. Biol.* **202** 2393

Drucker E G and Lauder G V 2000 A hydrodynamic analysis of fish swimming speed: wake structure and locomotor force in slow and fast labriform swimmers *J. Exp. Biol.* **203** 2379

Drucker E G and Lauder G V 2001a Wake dynamics and fluid forces of turning maneuvers in sunfish *J. Exp. Biol.* **204** 431

Drucker E G and Lauder G V 2001b Locomotor function of the dorsal fin in teleost fishes: experimental analysis of wake forces in sunfish *J. Exp. Biol.* **204** 2943

Drucker E G and Lauder G V 2002 Experimental hydrodynamics of fish locomotion: functional insights from wake visualization *Integ. Comp. Biol.* **42** 243–57

Gibb A, Jayne B C and Lauder G V 1994 Kinematics of pectoral fin locomotion in the bluegill sunfish *Lepomis macrochirus J. Exp. Biol.* **189** 133

Isogai K, Shinmoto Y and Watanabe Y 1999 Effects of dynamic stall on propulsive efficiency and thrust of flapping foil *AIAA J.* **37** 1145–51

Jayne B C, Lozada A and Lauder G V 1996 Functions of the dorsal fin in bluegill sunfish: motor patterns during four distinct locomotor behaviors *J. Morphol.* **228** 307–26

Kotapati R B, Mittal R and Cattafesta L N III 2006 Numerical experiments in synthetic jet based separation control *AIAA 2006-0320 (Reno, NV)*

Lauder G V 2005 *The Physiology of Fishes* 3rd edn ed D H Evans and J B Claiborne (Boca Raton, FL: CRC Press) pp 3–46

Lauder G V, Drucker E G, Nauen J and Wilga C D 2003 *Vertebrate Biomechanics and Evolution* ed V Bels, J-P Gasc and A Casinos (Oxford: Bios Scientific) pp 117–35

Lauder G V, Madden P, Hunter I, Tangorra J, Davidson N, Proctor L, Mittal R, Dong H and Bozkurttas M 2005 Design and performance of a fish fin-like propulsor for AUVs *Proc. 4th Int. Symp. on Unmanned Untethered Submersible Technology (UUST)*

Lauder G V, Madden P, Mittal R, Dong H and Bozkurttas M 2006 Locomotion with flexible propulsors: I. Experimental analysis of pectoral fin swimming in a sunfish *Bioinspiration Biomimetics* **1** S25–34

Lauder G V, Nauen J and Drucker E G 2002 Experimental hydrodynamics and evolution: function of median fins in ray-finned fishes *Int. Comp. Biol.* **42** 1009

Lewin G C and Haj-Hariri H 2003 Modeling thrust generation of a low dimensional heaving airfoil in a viscous flow *J. Fluid Mech.* **492** 339–62

Maxworthy T 1979 Experiments on the Weis-Fogh mechanism of lift generation by insects in hovering flight: part I. Dynamics of the ‘fling’ *J. Fluid Mech.* **93** 47–63

Mittal R 2004 Computational modeling in bio-hydrodynamics: trends, challenges and recent advances *IEEE J. Oceanic Eng.* **29** 595–604

Mittal R, Akhtar I, Bozkurttas M and Najjar F M 2003 Towards a conceptual model of a bio-robotic AUV: pectoral fin hydrodynamics *Proc. 13th Int. Symp. on Unmanned Untethered Submersible Technology (UUST)*

Mittal R, Dong H, Bozkurttas M, Loebbecke A and Najjar FM 2006 Analysis of swimming and flying in nature using an immersed boundary method *AIAA-2006-2867: 36th AIAA Fluid Dynamics Conf. and Exhibit (San Francisco, CA, 5–8 June)*

Mittal R and Iaccarino G 2005 Immersed boundary methods *Ann. Rev. Fluid Mech.* **37** 239–61

Ramamurti R, Sandberg W C, Löhner R, Walker J A and Westneat M W 2002 Fluid dynamics of flapping aquatic flight in the bird wrasse: 3-D unsteady computations with fin deformation *J. Exp. Biol.* **205** 2997–3008

Soria J and Cantwell B J 1993 Identification and classification of topological structures in free shear flows *Eddy Structure Identification in Free Turbulent Shear Flows* ed J P Bonnet and M N Glauser pp 379–90

Tangorra J L, Davidson S N, Hunter I W, Madden P W, Lauder G V, Dong H, Bozkurttas M and Mittal R 2006 The development of a biologically inspired propulsor for unmanned underwater vehicles *IEEE J. Ocean Eng.* submitted

Triantafyllou M S, Techet A H and Hover F S 2004 Review of experimental work in biomimetic foils *IEEE J. Ocean Eng.* **29**

Van Dyke M 1988 *An Album of Fluid Motion* (Stanford, CA: The Parabolic Press)